Hydrodynamic load modeling and analysis of a floating bridge in homogeneous wave conditions ⋆

Zhengshun Cheng[a,b,c,*], Zhen Gao[a,b,c], Torgeir Moan[a,b,c]

[a] *Department of Marine Technology, Norwegian University of Science and Technology (NTNU), Trondheim, 7491, Norway*
[b] *Centre for Ships and Ocean Structures (CeSOS), NTNU, Trondheim, 7491, Norway*
[c] *Centre for Autonomous Marine Operations and Systems (AMOS), NTNU, Trondheim, 7491, Norway*

Abstract

The Norwegian Public Road Administration (NPRA) is currently developing the E39 ferry-free project, in which several floating bridges will be built across deep and wide fjords. In this study, we consider the floating bridge that was an early concept for crossing the Bjørnafjorden with a width of about 4600 m and with a depth of more than 500 m. The floating bridge concept is a complex end-anchored curve bridge, consisting of a cable-stayed high bridge part and a low bridge part supported by 19 pontoons. It has a number of eigen-modes, which can be excited by wave loads. Wave loads and their effects should thus be properly modeled and assessed. Therefore, the effect of hydrodynamic load modeling are investigated in homogeneous wave conditions, including varying water depth at the ends of the bridge, viscous drag force on pontoons, short-crestedness and second order wave loads. It is found that the varying water depth has negligible effect, while the other features are important to consider. Second order difference-frequency wave loads contribute significantly to sway motion, axial force and strong axis bending moments along the bridge. However, these effects can be reduced by viscous drag forces, which implies that an appropriate model of viscous drag force effect on the pontoons is important. short-crested

*Corresponding author.
Email address: zhengshun.cheng@ntnu.no, zhengshun.cheng@gmail.com
⋆Prof. Masahiko Fujikubo serves as editor for this article.

waves greatly affect the heave motion and weak axis bending moment. All these considerations on hydrodynamic load modeling are further applied to analyze the wave load effect of a floating bridge in a fjord considering inhomogeneous waves [1].

Keywords: floating bridge, wave load, load effect, short-crested, second order wave loads

---

1. Introduction

The Norwegian Public Road Administration (NPRA) is developing the European highway E39 ferry-free project, in which the deep and wide Norwegian fjords will be connected by bridges, instead of by ferries. Due to very large depth (up to 1300 m) and width (up to about 6 km) of these fjords, floating bridges are favorable from an economic point of view. The site considered in this study is the Bjørnafjorden located on the west coast of Norway, as shown in Fig. 1(a). It has a width of about 4600 m and a water depth in the middle of Bjørnafjorden of more than 500 m.

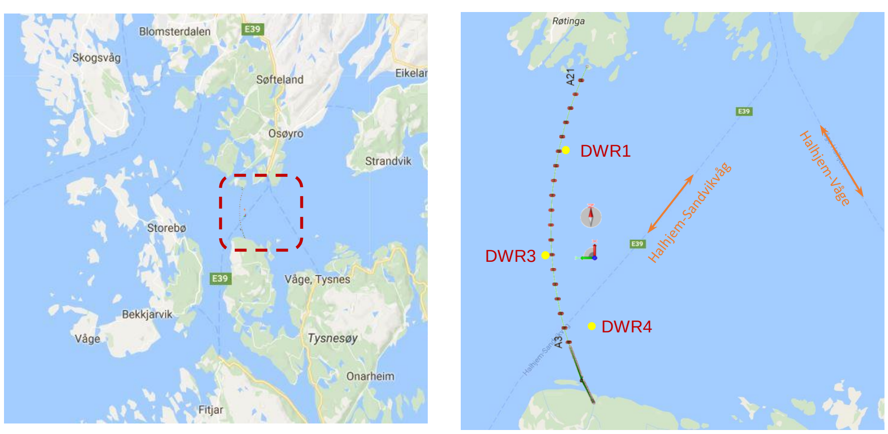

(a) The Bjørnafjorden

(b) Floating bridge

Figure 1: (a) Potential site for a floating bridge in Bjørnafjorden. (b) An end-anchored curved floating bridge model across the Bjørnafjorden. The approximate position of three Datawell Directional Wave Riders (DWRs) is also marked.

Several floating bridge concepts have been proposed for the crossing of Bjørnafjorden, including submerged floating tube bridge concept, cable stayed bridge with towers supported by TLP (tension leg platform) concept, side-anchored straight pontoon supported floating bridge concept, and end-anchored curved pontoon supported floating bridge concept [2]. Among them the end-anchored curved floating bridge concept is considered in this study, as shown in Figs. 1(b), 2 and 3. One main advantage of this concept is that it avoids the use of mooring system in deep water, since it can carry transversal loads through arch action. Currently there are two existing floating bridge in Norway, i.e. the Bergsøysund bridge close to Kristiansund, and the Nordhordlands bridge North of Bergen. Both these two bridge adopted the curved, end-anchored design.

The floating bridge supported by pontoons is a kind of Very Large Floating Structures (VLFSs). Hydroelastic behavior of VLFSs has been numerically investigated by many researchers. Three approaches are usually used for hydroelastic analysis of VLFSs, i.e. the modal superposition method [3, 4, 5], the direct method [6], and the discrete-module based method [7, 8]. In addition, several studies are especially carried out to investigate dynamic responses of floating bridges in fjords. Based on the multi-mode theory, Kvåle et al. [9] developed a method in the frequency domain to account for the hydroelastic responses of pontoon type floating bridges, and applied it to investigate the dynamic behavior of Bergsøysund bridge. Lie et al. [10] investigated the feasibility of deploying an end-anchored floating bridge in Masfjorden and compared its dynamic response with a submerged floating tube bridge concept. Fredriksen et al. [11] studied the hydrodynamic aspects of pontoon optimization for a side-anchored floating bridge. The bottom flange, geometrical shaping and length of pontoon are recommended to be specially chosen to decrease the bridge response. In addition, model test of a pontoon type floating bridge in wave basin was carried out in 1989 at MARINTEK (Now SINTEF OCEAN), and numerical results based on potential flow theory presented fairly good agreements with those from the model test [12].

However, the floating bridge concept considered in this study is more complex and challenging than those mentioned above. As described in detail in Section 2, the bridge concept is very long, and includes a cable-stayed high bridge part and a pontoon supported floating bridge part. It has a number of eigen-modes that might be excited by environmental loads, for instance wave loads. The waves in the fjord are mainly generated by local wind. Numerical simulations and field measurements have confirmed that these waves are quite different from waves in the open sea. Hence, proper modeling of these wave loads and their effects is important.

This study comprehensively investigated several modeling aspects of hydrodynamic loads for the considered floating bridge concept, including varying water depth, viscous drag forces, short-crested waves and second order wave loads. It was carried out by assuming a homogeneous wave condition; however, it can provide recommendations on the modeling of wave loads and wave load effects on a complex floating bridge in a fjord. This study is further extended by considering more realistic inhomogeneous wave conditions [1].

2. Floating bridge concept

The floating bridge concept considered in this study, as shown in Figs. 2 and 3, was designed for crossing Bjørnafjorden. It is anchored at both ends and has a bridge girder curved in the horizontal plane, with a radius of 5000 m and with a total length of approximately 4600 m. The bridge girder is continuous so that it can carry transverse loads through arc actions. This is also the idea of the curve design of this floating bridge concept. Additionally, the bridge girder is a Vierendeel beam, consisting of two parallel steel boxes connected by crossbeams.

This bridge concept includes a high bridge part and a floating bridge part. The high bridge is cable-stayed located in the south and is designed for ship navigation. It has a main span of 490 m and a back span of 370 m. A total of 80 cables are used to carry the girder. The floating bridge part is supported by 19 pontoons with a span of 197 m. It can also be divided in to a high part and a low part, where the high part is used to smoothly connect the main span

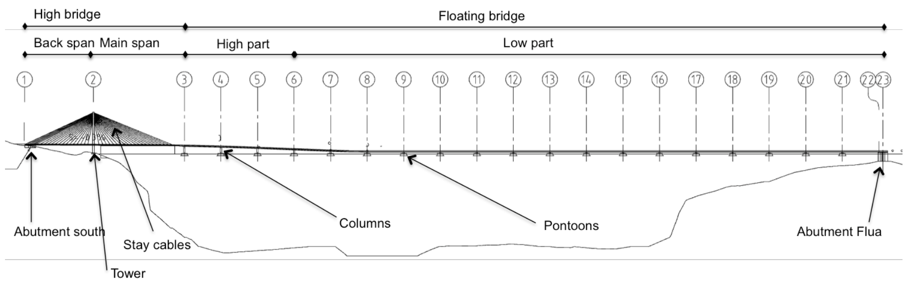

Figure 2: The end anchored curved floating bridge concept [13].

and the low part, as illustrated in Fig. 2. The bridge girder is supported by pontoons through columns. In general, the bridge concept is characterized by 23 locations based on the location of tower and pontoons, as shown in Fig. 2. These 23 locations are represented by A1, A2, ..., A23 in this study.

The bridge girder is monolithically connected to the abutment in South and to the abutment at Flua in North. The abutment in South is a fixed concrete caisson with a length of 60 m. It is heavy enough to provide sufficient friction capacity on the rock foundation. However, for the abutment at Flua in North, it is concrete caisson built on a water depth of 40 m. It is filled with ballast in order to withstand the huge end moments from the bridge girder. The tower consists of a single concrete column. The transversal support between tower and bridge deck is introduced to reduce the bending moments in the abutment in South.

The pontoons are made of light weight concrete and the corresponding submerged parts are watertight. The displacement of each pontoon is approximately 18000 tons. More main data of the pontoons are given in Table 1.

3. Description of wave field in a fjord

Due to the complex topography, waves in a fjord are quite different from waves in the open sea. The waves in a fjord, for in stance in Bjørnafjorden, usually consist of two parts: swell from the ocean and waves generated by local winds. To characterize the wave condition in Bjørnafjorden, both field measure-

Table 1: Main parameters of pontoon [13]

Length	m	28
Width	m	68
Height	m	14.5
Freeboard	m	4
Draft	m	10.5
Mass	ton	11300
Center of gravity	m	(0, 0, -4.2)
Roll inertia I_{44}	$ton \cdot m^2$	49000
Pitch inertia I_{55}	$ton \cdot m^2$	13600
Yaw inertia I_{66}	$ton \cdot m^2$	57000
Displacement	ton	18300
Center of buoyancy	m	(0, 0, -5.37)
Roll waterplane stiffness	MNm/rad	5700
Pitch waterplane stiffness	MNm/rad	1000
Heave stiffness	MN/m	17.5

ments and numerical simulations have been conducted by the NPRA. The measured wave data has been analyzed by Cheng et al. [14]. Numerical simulations were carried out by Norconsult [15], which dealt with the swell and wind generated waves separately. It has been revealed that swell is fairly small and wind generated waves are much larger. Based on hindcast wind data in Bjørnafjorden from 1979 to 2015, the 100-year wind waves were estimated, as given in Table 2. Numerical simulations also indicated that waves are short-crested and the wave spectrum at a given point in Bjørnafjorden can be described by the JONSWAP spectrum.

Table 2: 100-year wind waves in Bjørnafjorden [16]

Sectors	H_s [m]	T_p [s]
345°- 75°	1.5	5.0
75° - 105°	2.8	6.6
105° - 165°	1.6	5.3
165° - 225°	1.9	5.3
225° - 315°	2.4	5.9
315° - 345°	2.5	6.2

Hence, the short-term sea state, for instance in every 3 hours, can be considered to be Gaussian and stationary, the wave elevation at point (x, y) can be expressed as a sum of all component waves from different directions,

$$\zeta\left(x,y,t\right)=\Re\sum_{n=1}^{N}\sum_{m=1}^{M}\sqrt{2S_{\zeta}(\omega_n,\theta_m)\Delta\omega\Delta\theta}\exp\left[i\left(\omega_n t-k_n x\cos(\theta_m)-k_n y\sin(\theta_m)+\epsilon_{nm}\right)\right] \tag{1}$$

Here N and M are the total number of wave frequency components and wave direction components respectively. ϵ_{nm} is the random phase angle uniformly distributed within $[0, 2\pi)$, x and y are the coordinates of the floater, θ is wave direction angle, and k is wave number and is related to the wave frequency through the dispersion relation. $S_\zeta(\omega, \theta)$ denotes the directional wave spectrum and is a function of frequency and wave direction.

$$S_\zeta(\omega,\theta)=S(\omega)D(\omega,\theta) \tag{2}$$

where $S(\omega)$ is the unidirectional wave spectrum and $D(\omega, \theta)$ symbolizes the direction distribution. The directional function for locally generated sea states is commonly approximated as independent of frequency, i.e. $D(\omega, \theta) = D(\theta)$. In this study, the unidirectional wave spectrum used is the JONSWAP spectrum defined as [17],

$$S(\omega)=\frac{\alpha g^2}{\omega^5}\exp\left[-\beta\left(\frac{\omega_p}{\omega}\right)^4\right]\gamma^{\exp\left(\frac{(\omega/\omega_p-1)^2}{2\sigma^2}\right)} \tag{3}$$

where

$$\alpha=5.061\frac{H_s^2}{T_p^4}\left(1-0.287\ln(\gamma)\right) \tag{4}$$

$$\omega_p=\frac{2\pi}{T_p} \tag{5}$$

$$\sigma=\begin{cases}0.07 & \text{for } \omega<\omega_p\\ 0.09 & \text{for } \omega\geq\omega_p\end{cases} \tag{6}$$

in which α is the spectral parameter, β is the form parameter and is chosen to be 1.25, γ is the peakedness parameter and according to the metocean design basis [16] it is estimated from

$$\gamma = \begin{cases} 5 & \text{for } \frac{T_p}{\sqrt{H_s}} \le 3.6 \\ \exp\left(5.75 - 1.15\frac{T_p}{\sqrt{H_s}}\right) & \text{for } 3.6 < \frac{T_p}{\sqrt{H_s}} < 5 \\ 1 & \text{for } 5 \le \frac{T_p}{\sqrt{H_s}} \end{cases} \tag{7}$$

The directional distribution takes the cos-s distribution, as follows.

$$D(\theta) = \frac{\Gamma(1+s/2)}{\sqrt{\pi}\Gamma(1/2+s/2)} \cos^s(\theta - \theta_p) \tag{8}$$

where s is the spreading exponent, and is set to be 4 for short-crested waves [16] in this study. θ_p is the main wave direction and $|\theta - \theta_p| \le \pi/2$.

Hence, the wave elevation at point (x, y) is related to wave spectrum $S(\omega)$, directional distribution $D(\theta)$, and random phase angle ϵ_{nm}. When the types of wave spectrum and directional distribution are determined, the wave elevation at point (x, y) can be regarded as a function of significant wave height H_s, peak period T_p, main wave direction θ_p and random phase angle ϵ_{nm}.

For the floating bridge concept considered in this study, the wave elevations or wave spectra at 19 pontoons are required in order to investigate the dynamic responses of the floating bridge. In this study, it is assumed that the wave field in Bjørnafjorden is homogeneous, which implies these aforementioned four parameters (H_s, T_p, θ_p, ϵ_{nm}) are identical for all pontoons. This assumption is reasonable since this study focuses on the hydrodynamic load modeling of this complex floating bridge. However, both the field measurements and numerical simulations reveal that these four parameters at different pontoons are to some extent different, i.e. the wave field is inhomogeneous. The effect of inhomogeneous waves on the dynamic responses of the floating bridge is addressed comprehensively by Cheng et al. [1].

4. Methodology

4.1. Numerical model of the floating bridge

A numerical model of the floating bridge concept, as shown in Fig. 3, was bulit using the software SIMO-RIFLEX [18, 19], which is developed by MAR-

INTEK and has been widely used in the analyses of offshore platforms and wind turbines. In general, RIFLEX [18] is a non-linear finite element solver and SIMO [19] is a solver that can account for various kinds of hydrodynamic loads based on coefficients from a potential flow code.

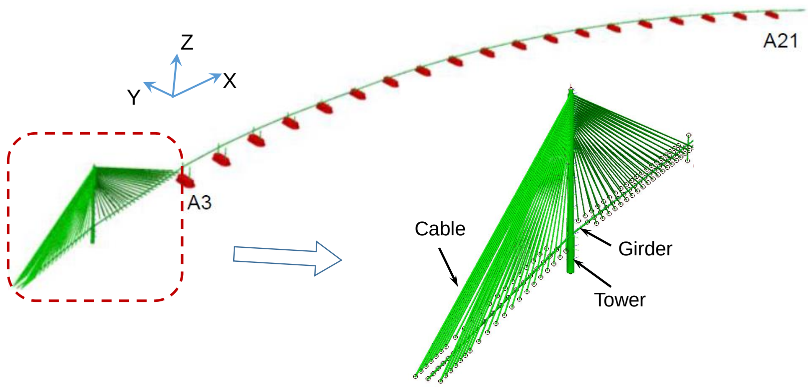

Figure 3: The end anchored curved floating bridge model including a cable stayed high bridge and a pontoon supported low bridge.

RIFLEX is able to model the system by use of beam and bar elements based on small strain theory. Stiffness contribution from nonlinear geometries is considered in the present study. The girder, tower, and columns were modeled as nonlinear beam elements. The cables were represented as nonlinear bar elements, while the pontoons were modeled as rigid bodies. For the mesh size, the element length varies from 10 m to 15 m for the girder, from 5 m to 8 m for the columns, and from 30 m to 40 m for the cables, depending on the locations. The structural properties of typical sections of the bridge girder are given in Table 4, in which the location of typical sections are indicated in Table 3. Here the detailed properties of the columns, cables and tower are not presented, but they are described in the report by COWI [13]. It should be noted that in the original design, the bridge girder consisted of two parallel steel boxes connected by crossbeams, while in the numerical model, it was simplified as an equivalent beam. The structural damping was also considered by using the Rayleigh damping, in which the mass and stiffness proportional coefficients are $\mu = 0.0005$ and

$\lambda = 0.03$, respectively. Therefore for different response frequency ω, the damping ratio ξ relative to critical damping is given by

$$\xi = 0.5(\mu/\omega + \lambda\omega) \tag{9}$$

The structural damping ratio corresponding to the first and second eigen-modes of the floating bridge (see Table 6) is approximately 1.42% and 0.84%, respectively. The dynamic equilibrium equation the dynamic equilibrium equations is solved in the time domain using the Newmark-β numerical integration ($\beta_{num} = 0.256$, $\gamma_{num} = 0.505$). The time step used is 0.01 s for all simulations.

Table 3: Location of different cross-sectional properties for the bridge girder [13]. Here H1, H2, H3, S1 and F1 represent different cross sections, and the corresponding properties are given in Table 4.

Cross-section	Roadline
Stiff bridge (abutment)	S=0m to S=60m
H1	S=60m to S=220m
H2	S=220m to S=345m
H3	S=345m to S=395m
H2	S=395m to S=520m
H1	S=520m to S=850m
S1	S=850m to S=860m
S1(24.62m) - F1(147.74m) - S1(24.62m)	S=860m to S=4602.74m

Table 4: Structural properties of the bridge girder [13]

		High bridge			Floating bridge	
		H1	H2	H3	S1	F1
Mass	$[ton/m]$	23.96	29.05	33.13	31.8	26.71
EA	$[kN]$	3.07E+08	4.41E+08	5.52E+08	5.25E+08	3.89E+08
EI_z	$[kNm^2]$	1.16E+11	1.70E+11	2.12E+11	2.18E+11	1.55E+11
EI_y	$[kNm^2]$	1.28E+09	1.97E+09	2.46E+09	3.85E+09	2.76E+09
GI_x	$[kNm^2]$	1.42E+09	1.98E+09	2.48E+09	3.70E+09	2.90E+09

Note that I_y and I_z represent the second area moment about the strong axis and weak axis of the girder, respectively. I_x denotes the torsion constant.

Modeling of hydrodynamic loads due to waves is described in detail in Section

4.2. Wind and current loads were not considered in this study. Regarding the boundary condition, two ends of the bridge and the tower bottom were fixed. The connection point between the girder and the tower had fixed degree of freedom in transverse direction (sway). Master-slave rigid connection was applied between cable ends and girder, between girder and columns, and between pontoons and columns. The pretension in each cable was also accounted for in the numerical model.

Fig. 4(a) depicts the definition of rigid body motion modes for the pontoons. The reference point is located at the center of waterplane area of the pontoon. The global coordinate system is defined as shown in Fig. 4(b). X is positive in the north direction, Y is positive in the west direction, and Z is positive upward. The origin is located at the water plane at the south end. The incoming wave directions are also indicated in Fig. 4(b).

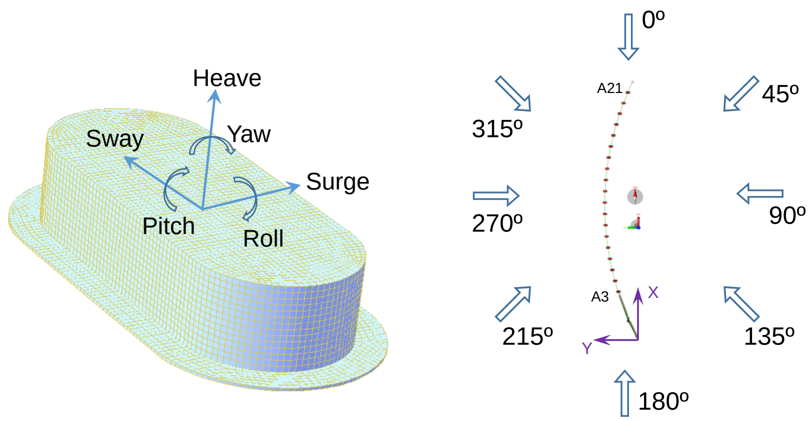

(a) Rigid body motion modes of the pontoon

(b) Global coordinate system

Figure 4: (a) definition of rigid body motion modes of the pontoon (b) definition of global coordinate system and wave incoming directions. Note that the fjord boundary condition is not plotted here.

4.2. Modeling of hydrodynamic loads

In SIMO, the pontoons were regarded as large volume structures. Their hydrodynamic coefficients, such as added mass, radiation damping, and first-order wave excitation force, etc., were first estimated based on the potential flow theory [20]. The hydrodynamic interaction between adjacent pontoons were not considered, since the spacing between adjacent pontoons are more than 4 times the typical wave length under 100-year wave condition. The wall effect due to fjord sides on the hydrodynamic coefficients was not considered either.

The added mass and radiation damping were then applied as radiation forces in time domain using the convolution technique [21], and the dynamics of the pontoon can be represented using the equation of motion as follows.

$$\sum_{k=1}^{6}\left[\left(M_{jk}+A_{jk}^{\infty}\right)\ddot{x_k}\left(t\right)+\int_{-\infty}^{\infty}\kappa_{jk}\left(t-\tau\right)\dot{x_k}\left(\tau\right)d\tau+\left(K_{jk}^{g}+K_{jk}^{h}\right)x_k\left(t\right)\right]=F_j^{exc}\left(t\right) \tag{10}$$

where j and k are degree of freedom $(j,k=1,2,...,6)$, M_{jk} is the mass of the pontoon, A_{jk}^{∞} is the infinite-frequency added mass, $x_k\left(t\right)$, $\dot{x_k}\left(t\right)$ and $\ddot{x_k}\left(t\right)$ are the displacement, velocity and acceleration of the pontoon, respectively. $\kappa_{jk}\left(t-\tau\right)$ is the retardation function which represents the fluid memory effect. K_{jk}^{h} is the hydrostatic restoring and K_{jk}^{g} is the nonlinear restoring resulting from the bridge girder. $F_j^{exc}\left(t\right)$ is the excitation forces which includes the first order force $F_j^{1}\left(t\right)$, second order mean, rapidly varying and slowly varying wave drift force $F_j^{2}\left(t\right)$ and viscous force $F_j^{Drag}\left(t\right)$.

$$F_j^{exc}\left(t\right)=F_j^{1}\left(t\right)+F_j^{2}\left(t\right)+F_j^{Drag}\left(t\right) \tag{11}$$

In Eq. 10, only the right hand side of equation, i.e. the wave excitation force $F_j^{exc}\left(t\right)$, is related to the incident wave condition. The viscous drag forces on the pontoons were incorporated through the Morison's equation by considering only the quadratic viscous drag term. The transverse viscous force per unit length is given by

$$dF_j^{Drag}\left(t\right)=\frac{1}{2}\rho_w C_d D(u_w-u_b)\left|u_w-u_b\right)| \tag{12}$$

where ρ_w is the water density, u_w is the transverse wave particle velocity, u_b is the local transverse body velocity, D is the characteristic width of the body, and C_d is the quadratic drag coefficient. The first order force and second order force can be expressed as a function of wave force transfer function and wave elevation. The generation of first-order and second-order wave excitation forces will be addressed in the next section.

Regarding the fully coupled time domain analysis, at each time step, the dynamic equilibrium equations of the floating bridge system, including the tower, cables, girder, columns and pontoons, were solved in RIFLEX. Then the platform motion was transfered to SIMO to update the hydrodynamic loads acting on the pontoons.

4.3. Generation of wave excitation forces

4.3.1. First order wave forces

In linear potential flow theory, the first order wave transfer function, denoted by $H_j^{(1)}(\omega,\theta)$, can be estimated in frequency domain. It represents the force generated by a unit regular wave associated with frequency of ω and propagation direction of θ. Hence the total first order wave force can be estimated in time domain by

$$F_j^1(x,y,t) = \Re\sum_{n=1}^{N}\sum_{m=1}^{M}\left|H_j^{(1)}(\omega_n,\theta_m)\right|\sqrt{2S_\zeta(\omega_n)D(\theta_m)\Delta\omega\Delta\theta} \\ \exp\left[i\left(\omega_n t - k_n x\cos(\theta_m) - k_n y\sin(\theta_m) + \epsilon_{nm} + \phi_{H_{jnm}^{(1)}}\right)\right] \tag{13}$$

where $\phi_{H_{jnm}^{(1)}}$ denotes the phase angle of the first order wave force transfer function $H_j^{(1)}(\omega,\theta)$.

Upon deriving the autocorrelation functions of Eq. 13 and using the Wiener-Kinchin relation, the spectra of the first order wave force can be obtained, as follows

$$S_{F_j^{(1)}}(\omega) = \int_{-\pi}^{\pi} H_j^{(1)}(\omega,\theta)\, S_\zeta(\omega)D(\theta)H_j^{(1)*}(\omega,\theta)\,d\theta \tag{14}$$

where the asterisk (*) represents the complex conjugate. For long-crested waves, the spectra of first order wave force is simplified as

$$S_{F_j^{(1)}}(\omega) = H_j^{(1)}(\omega)\, S_\zeta(\omega) H_j^{(1)*}(\omega) \tag{15}$$

Before carrying out the time domain simulations, the time series of wave excitation forces are required to be generated based on the mean position of each pontoon. It can be achieved by applying inverse Fast Fourier Transform (IFFT) on the basis of Eq. 14 for short-crested waves and Eq. 15 for long-crested waves.

4.3.2. Second order wave forces

The first two eigen-periods listed in Table 6 are very large, which implies that these modes might be excited by second order difference-frequency wave forces. In this study, the second order wave force is thus considered. In short-crested seas, the waves causing second order difference-frequency wave force can come from different directions. For simplicity this direction interaction effect is ignored in this study. The second order difference-frequency wave force in the time domain can be expressed by

$$\begin{aligned} F_j^2(x,y,t) = \Re \sum_{n=1}^{N}\sum_{l=1}^{N}\sum_{m=1}^{M} \left| H_j^{(2-)}(\omega_n,\omega_l,\theta_m)\right| \sqrt{2S_\zeta(\omega_n)D(\theta_m)\Delta\omega\Delta\theta} \\ \sqrt{2S_\zeta(\omega_l)D(\theta_m)\Delta\omega\Delta\theta}\exp\left[i\left((\omega_n-\omega_l)t+\epsilon_{nm}-\epsilon_{lm}+\phi_{H^{(2)}_{jnlm}}\right)\right] \end{aligned} \tag{16}$$

where $H_j^{(2-)}(\omega_n,\omega_l,\theta_m)$ symbols the quadratic transfer function (QTF) of difference-frequency wave force, and $\phi_{H^{(2)}_{jnlm}}$ denotes its phase angle. An approach for accurately modeling the second-order difference-frequency wave forces is to estimate the QTF for a number of directions; however, this is very time consuming and QTF depends on the first order motions which might be difficult to get considering the motion coupling between bridge girder and pontoons. It is then simplified by applying the Newman's approximation. It implies that $\phi_{H^{(2)}_{jnlm}} = 0$

and

$$H_j^{(2-)}(\omega_n, \omega_l, \theta_m) = \frac{1}{2}\left[H_j^{(2-)}(\omega_n, \omega_n, \theta_m) + H_j^{(2-)}(\omega_l, \omega_l, \theta_m)\right] \tag{17}$$

For each pontoon, only forces in surge, sway and moment in yaw are modeled. Similar to the first order wave force spectra, the spectra of second order difference-frequency wave forces can also be derived, as follows

$$S_{F_j^{(2)}}(\mu) = 8\int_0^{\infty}\int_{-\pi}^{\pi}\int_{-\pi}^{\pi} H_j^{(2-)}(\omega, \omega+\mu, \theta)\, S_\zeta(\omega)D(\theta)S_\zeta(\mu-\omega)D(\theta)H_j^{(2-)*}(\omega, \omega+\mu, \theta)\, d\theta d\theta d\omega \tag{18}$$

4.3.3. Verification

An example of time series of the generated first order and second order wave forces in sway is shown in Fig. 5. The corresponding short-crested wave condition is $H_s = 3$ m, $T_p = 6$ s.

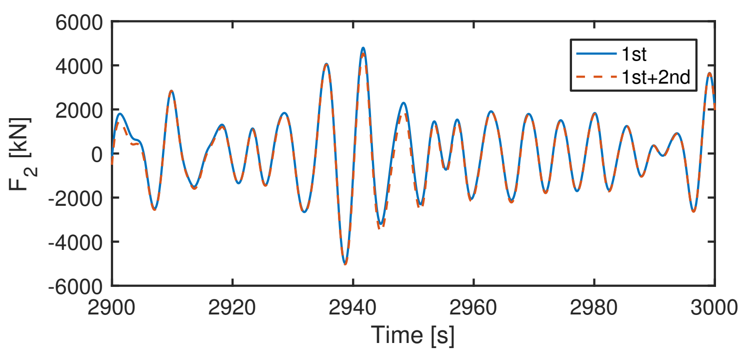

Figure 5: An example time history of the generated first order and second order wave excitation forces in sway.

To verify the accuracy of the generated time series, power spectral analyses were conducted for the wave elevation, first order wave force and second order wave force. These power spectra are then compared to those calculated in frequency domain. The spectra of wave elevation, first order sway force and second order sway force in frequency domain and time domain are compared, as shown in Fig. 6. It can be observed that the frequency domain results match very well with the time domain results.

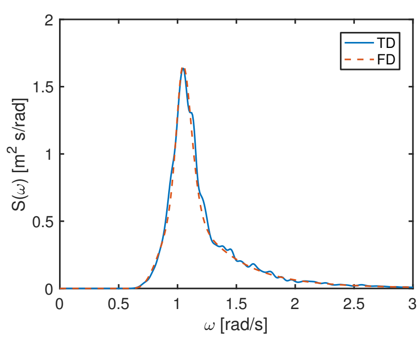

(a) Wave spectrum

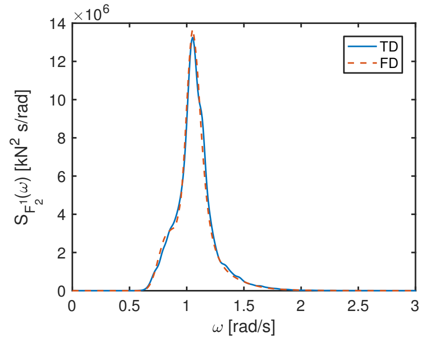

(b) Power spectrum of 1st order sway force

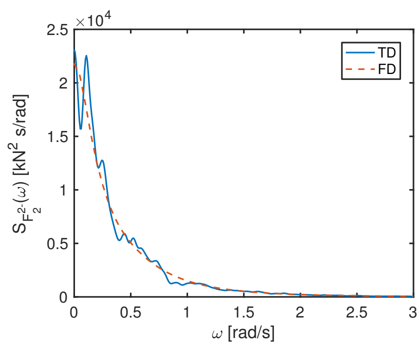

(c) Power spectrum of 2nd order sway force

Figure 6: Comparison of spectra of wave elevation, first order sway force and second order sway force in frequency domain and time domain.

5. Load cases and environmental conditions

In this study, a series of load cases (LCs), as given in Table 5, were defined to investigate the effects of different modeling aspects of hydrodynamic loads on the dynamic responses of the floating bridge, including varying water depth, viscous drag forces on the pontoons, short-crested waves and second order wave forces. LC2 and LC3 are used to identify the effect of viscous drag forces on the pontoons. The effect of short-crested waves and second order wave forces is investigated by LC1, LC2, LC4 and LC5 considering waves mainly from 270°, and by LC6, LC7 and LC8 considering waves mainly from 315°. The wave conditions considered are all homogeneous. Here we mainly consider the 100-

year wave condition coming from northwest, since a majority of waves with a large significant wave height are found from northwest when analyzing the measured wave data [14].

Table 5: Load cases for sensitivity studies.

	Wave force	Including viscous force	Wave crest	A3-A21			
				H_s [m]	T_p [s]	θ_p [°]	Spreading (s)
LC1	1st	No	Long-crested	2.4	5.9	270	-
LC2	1st+2nd	No	Long-crested	2.4	5.9	270	-
LC3	1st+2nd	Yes	Long-crested	2.4	5.9	270	-
LC4	1st	No	Short-crested	2.4	5.9	270	4
LC5	1st+2nd	No	Short-crested	2.4	5.9	270	4
LC6	1st	No	Long-crested	2.4	5.9	315	-
LC7	1st+2nd	No	Long-crested	2.4	5.9	315	4
LC8	1st+2nd	No	Short-crested	2.4	5.9	315	4

It should be noted that for each LC, 5 identical and independent simulations with different seeds were carried out. It is used to reduce the stochastic variation of dynamic responses. The statistical values and spectra presented in the following sections are based on the average of 5 seeds for each LC.

6. Results and discussion

6.1. Eigen-frequencies and eigen-modes

The eigen-frequencies and eigen-modes were first analyzed for the floating bridge system before carrying out time domain simulations. It is used to identify the critical eigen-modes and eigen-frequencies that might be excited by environmental loads. The first 20 eigen-periods and corresponding dominant motions are given in Table 6. It should be noted that when carrying out eigen-value analysis, the added mass from the pontoon are not properly incorporated due to the limitation of the codes. Therefore, differences are observed between the present eigen-value analysis results and those in [13], especially for the first mode. However, as given in later studies, the first four eigen-periods are identified from power spectra of dynamic responses, such as sway motion of the

Table 6: The first 20 eigen periods of the floating bridge model.

Mode	Period[1)] [s]	Frequency[1)] [rad/s]	Dominant[1)] motion	Period[2)] [s]	Error [%]	Period[3)] [s]	Error [%]
1	56.72	0.111	H	51.05	10.00	55.52	2.12
2	31.69	0.199	H	29.49	6.95	31.81	-0.38
3	22.68	0.277	H	22.46	0.99	23.07	-1.72
4	18.62	0.337	H	17.46	6.22	19.04	-2.26
5	14.33	0.439	H	13.40	6.47		
6	11.9	0.528	T	11.55	2.98		
7	11.48	0.547	T	11.46	0.18		
8	11.48	0.547	V	11.42	0.49		
9	11.02	0.571	V	11.40	-3.44		
10	10.95	0.574	V	11.39	-4.05		
11	10.95	0.574	V	11.38	-3.91		
12	10.94	0.574	V	11.34	-3.64		
13	10.92	0.576	V	11.26	-3.11		
14	10.89	0.577	V	11.15	-2.34		
15	10.81	0.581	V	10.99	-1.67		
16	10.71	0.587	V	10.88	-1.54		
17	10.64	0.591	V	10.72	-0.71		
18	10.48	0.600	V	10.44	0.40		
19	10.21	0.616	V	10.11	0.94		
20	9.88	0.636	V	10.04	-1.61		

[1)] the periods and frequencies are estimated by COWI [13], in which frequency dependent added mass are considered. Here H represents horizontal motion, T denotes torsional motion, and V symbols vertical motions.

[2)] the periods are estimated by eigen-value analysis by SIMO-RFILEX, in which frequency dependent added mass are not included.

[3)] these four periods are identified according the power spectra of dynamic responses from numerical simulations in this study, in which frequency dependent added mass are included.

bridge girder. The frequency-dependent added masses are all included in the time domain simulations. It is found that these four eigen-periods are fairly close to those in [13], indicating that the characteristics of eigen-periods for this floating bridge model match well with those in [13].

The first two eigen periods are respectively 55.5 s and 31.8 s, which cor-

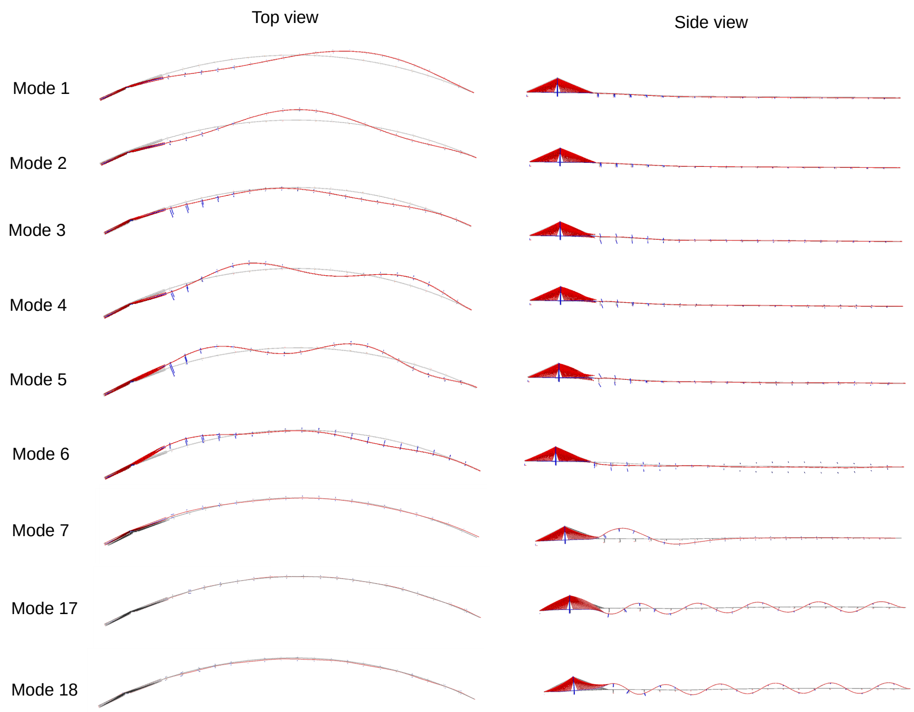

Figure 7: Several selected eigen-modes of the floating bridge based on eigen-value analysis by the SIMO/RIFLEX codes.

respond to horizontal motions and can be excited by second order difference frequency wave forces. The first five eigen modes are all dominated by horizontal motions, as shown in Fig. 7. There are about 20 eigen-modes that are dominated by vertical motions. They have a eigen-period ranging from 7.47 s to 11.48 s, which are due to heave motion of pontoons. Actually, the bridge concept considered has 19 pontoons; it indicates that there are a lot of combinations of heave motion from different pontoons, resulting in many eigen-modes dominated by vertical motions. For eigen-modes with a eigen-period ranging from 3.7 s to 7 s, the dominating motions are mainly torsional motions. More than 25 eigen-modes have a eigen-period below 3.7 s, in which the dominating motions are mainly pendulum motions, because of surge motion of pontoons.

6.2. Static responses of the floating bridge in calm water

The static structural responses along the floating bridge in calm water are studied in this section. Fig. 8 depicts the axial force, strong axis and weak axis bending moments along the bridge girder.

As illustrated in Fig. 2, the floating bridge concept is divided into the high bridge part and floating bridge part. The static loads between the high bridge part and floating bridge part differ a lot. Within the high bridge part, the axial force increases from almost zero at two ends (A1 and A3) to the maximum at A2. The strong axis and weak axis bending moments reach the maximum at A2 as well. Regarding the floating bridge part, the axial force is close to zero, and the weak axis bending moment varies significantly. The weak axis bending moment is due to the self weight of the bridge girder. Considering a section of bridge girder between two continuous axes, it can be simplified as a beam fixed at both ends, the bending moment reaches the maximum at two ends. In addition, the weak axis bending moment is one magnitude larger than the strong axis bending moment.

6.3. Effect of varying water depth at the ends of the bridge

As shown in Fig. 2, the sea floor terrain varies significantly in Bjørnafjorden; as a result, the water depth at each pontoon for the floating bridge is different. The water depth is approximately 500 m at pontoons located from axis A4 to A16, and it decreases to about 55 m at pontoon located at axis A21. These wavy terrain at the sea floor might affect the hydrodynamic coefficients of pontoons located at different axes (see Fig. 2). To study the effect of varying water depth, the hydrodynamic coefficients (added mass, potential damping, first order excitation force and mean drift force transfer function) of the pontoon were calculated in frequency domain at several different water depth, as plotted in Fig. 9. The transfer functions of first order wave excitation forces were estimated for waves coming from 270°. It should be noted here that though the calculation of hydrodynamic coefficients assumes a constant water depth, the results can still show the variation of hydrodynamic coefficients over water depth.

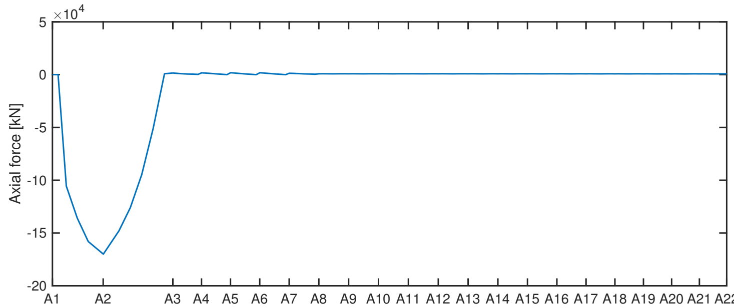

(a) Axial force

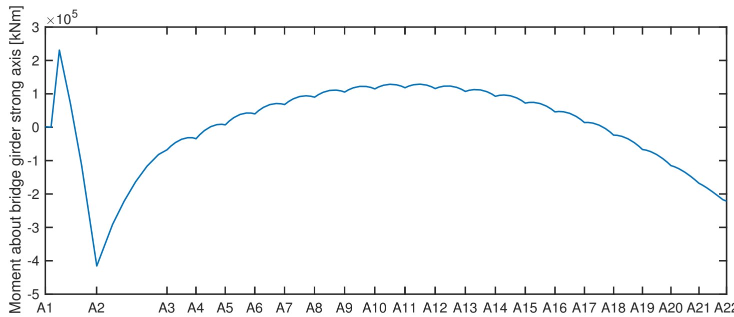

(b) Strong axis bending moment, M_z

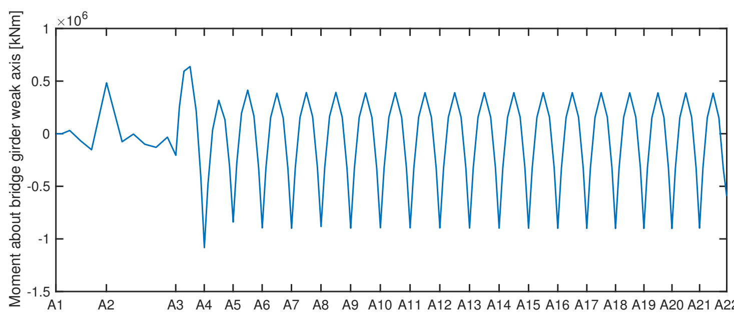

(c) Weak axis bending moment, M_y

Figure 8: Static structural responses along the floating bridge in calm water. (a) Axial force, (b) Strong axis bending moment, M_z, (c) Weak axis bending moment, M_y. Environmental loads are not considered.

The hydrodynamic interaction between adjacent pontoons were not considered, because they were well separated.

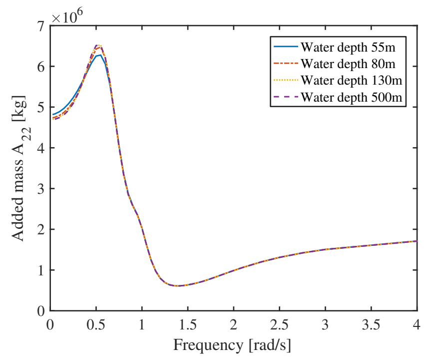

(a) Added mass, A_{22}

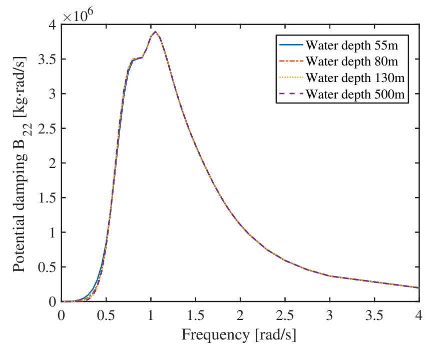

(b) Potential damping, B_{22}

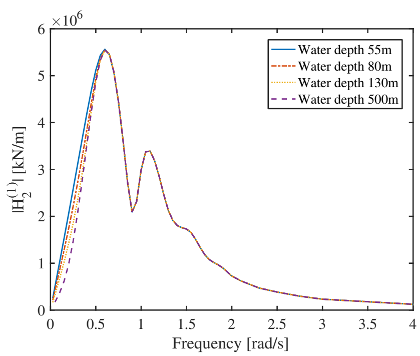

(c) RAO of first order excitation force, $H_2^{(1)}$

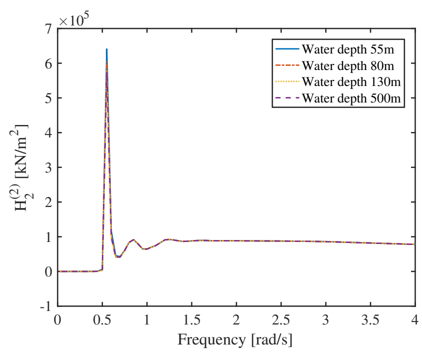

(d) Normalized mean drift force, $H_2^{(2)}$

Figure 9: Added mass, potential damping and transfer function of wave excitation forces of the pontoon. (a) Added mass, A_{22}, (b) Potential damping, B_{22}, (c) RAO of first order excitation force, $H_2^{(1)}$, (d) Normalized mean drift force, $H_2^{(2)}$. The transfer function of wave excitation force are estimated for waves coming from 270°.

It can be found in Fig. 9 that under different water depth, the added mass, potential damping, first order excitation force transfer function, and mean drift transfer function are identical for frequencies above approximately 0.6 rad/s, and differences are only visible for frequencies below 0.6 rad/s. For the 100-year wind waves given in Table 2, the energy of wave spectra is mainly located in the vicinity of 1.05 rad/s, and almost zero energy is located in frequencies below

0.6 rad/s, as shown in Fig. 6(a). Consequently, the first order wave excitation force will not be influenced by the varying water depth considered in the study. Neither does the mean drift force. This also indicates that the effect of varying water depth on the dynamic responses of the floating bridge is negligible.

6.4. Effect of viscous drag forces

This section gives a preliminary study on the effect of viscous drag forces on the dynamic responses of the floating bridge. The viscous drag forces were estimated by use of Eq. 12, in which the drag coefficients are key parameters. Currently no experimental data on the drag coefficients of such pontoon is available, a set of drag coefficients are assumed based on the report [13], that is $C_{dx} = 1$, $C_{dy} = 0.6$, and $C_{dz} = 2$. It should be noted that these values are taken conservatively, and realistic drag coefficients are expected to be larger. For instance the value $C_{dz} = 4.2$ was used by Xiang et al. [22] but it was also addressed that the validity of using such coefficient should be validated by model test.

Here the load cases considered are LC2 and LC3, in which the waves are long-crested and coming from west (270°). Both the first order and second order wave loads are studied. Numerical simulations with and without considering viscous drag forces on pontoons are conducted and the results are shown in Figs. 10 and 11. In general, the horizontal motion (sway) is significantly influenced by the viscous drag forces, while the vertical motion (heave) is not. Consequently, the horizontal motion induced structural responses, including axial force and strong axis bending moment along the bridge, are strongly affected by the viscous drag forces, while those induced by the vertical motion, such as weak axis bending moment and torsional motion, are not.

To identify the reason for such effects of the viscous drag forces, power spectral analyses are performed for several responses at representative locations. Fig. 12 shows the power spectra of various responses of girder node at A11 in LC2 and LC3. For the sway motion, the viscous drag forces have negligible effect on the wave frequency responses, and mainly affect the low-frequency responses in the vicinity of 0.2 rad/s, which corresponds to the second mode of the floating bridge. These low-frequency responses are caused by second order difference frequency wave forces. If the second order difference-frequency wave forces are not considered in the numerical simulations, the effect of the viscous drag forces on the sway will not be so notable. Similar trends are found in the power spectra of strong axis bending moment and axial force of girder node at A11 and at other locations. In contrast to the sway motion, the heave motion along the bridge is not sensitive to the viscous drag forces, so do the weak axis bending moment and torsional moment along the bridge.

6.5. Effects of short-crested waves and second order wave loads

Waves in the fjord driven by winds are likely to be short-crested. In numerical simulations, these waves can be modeled as long-crested or short-crested, and the second order wave loads can be considered or neglected. These model-

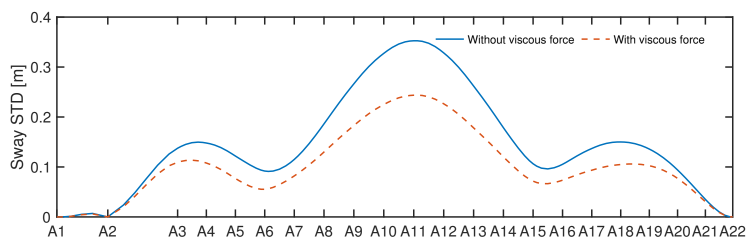

(a) Sway

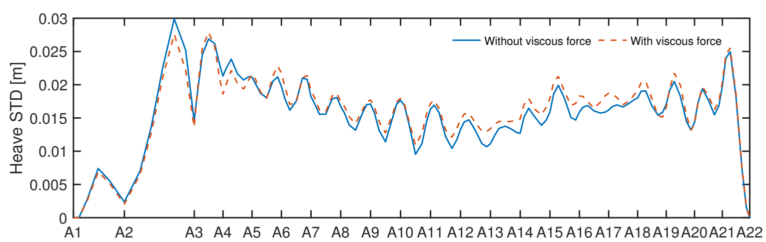

(b) Heave

Figure 10: The standard deviation of sway and motions along the bridge girder in LC2 and LC3 with and without considering the viscous drag forces. The waves are long-crested and second order wave loads are considered.

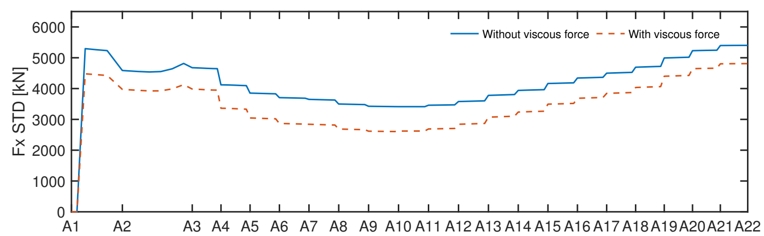

(a) Axial force, F_x

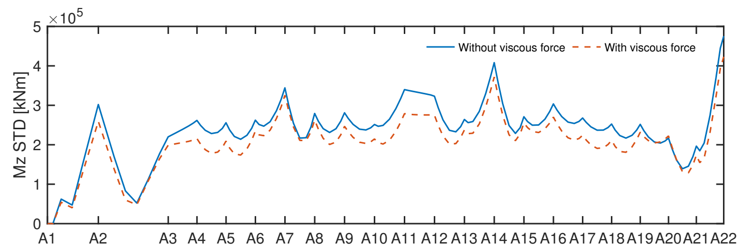

(b) Strong axis bending moment, M_z

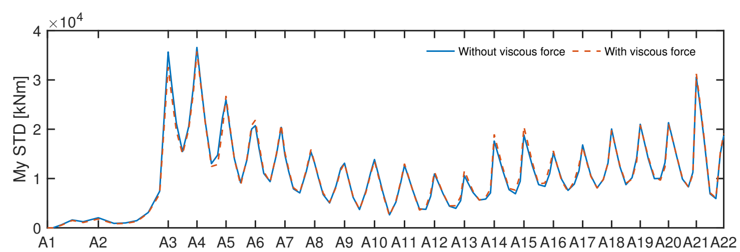

(c) Weak axis bending moment, M_y

Figure 11: The standard deviation of (a) axial force F_x (b) strong axis bending moment M_z, and (c) weak axis bending moment M_y, along the bridge girder in LC2 and LC3 with and without considering the viscous drag forces. The waves are long-crested and second order wave loads are considered.

ing differences can affect dynamic responses of the floating bridge. Therefore, these modeling aspects of hydrodynamic loads are studied in this section using LCs given in Table 5. Here LC1 and LC4 only consider first order wave load and LC2 and LC5 consider both first and second order wave loads. LC1 and LC2 consider long crest wave, and LC4 and LC5 consider short crest wave.

Fig. 13 shows the standard deviation of sway motion along the bridge girder.

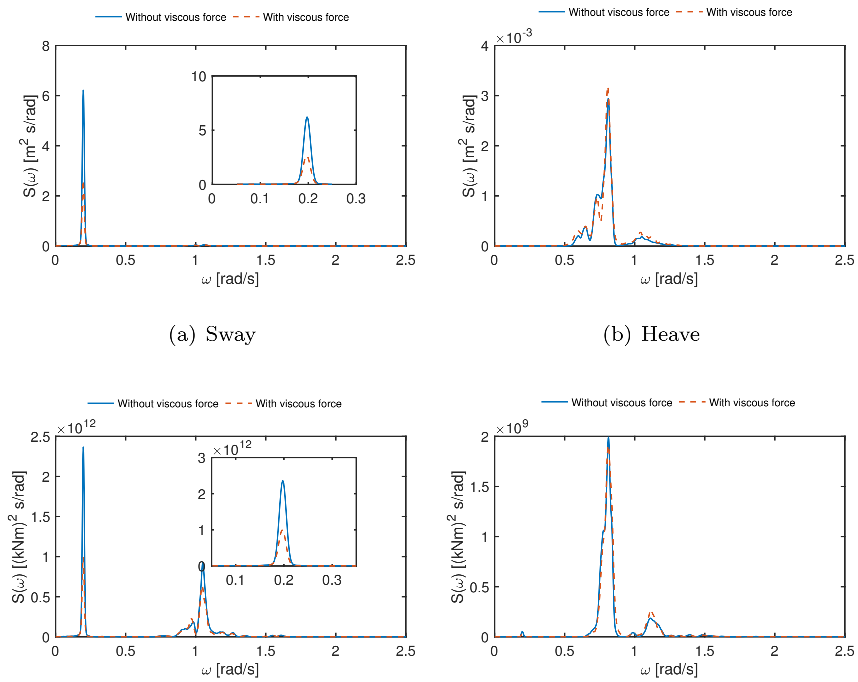

(a) Sway (b) Heave

(c) Strong axis bending moment, M_z (d) Weak axis bending moment, M_y

Figure 12: Power spectra of (a) sway motion, (b) heave motion, (c) strong axis bending moment and (d) weak axis bending moment of girder node at A11 in LC2 and LC3 with and without considering the viscous drag forces. The waves are long-crested and second order wave loads are considered.

When only considering first order wave loads (LC1 and LC4), the discrepancy with respect to sway standard deviation is relatively small between modeling with long-crested wave and with short-crested wave. However, when second order wave loads are considered (LC2 and LC5), this discrepancy is very significant. This means that the modeling of long-crested or short-crested waves matters a lot when the effect of second order wave loads is considered.

To reveal the reason for such discrepancy, power spectral analyses of sway motion were carried out for three typical nodes, i.e. at A3, A11, at A12 and at A16, as shown in Fig. 14. It can be found that at these four points, low-frequency resonant eigen modes are excited due to second-order difference-frequency wave

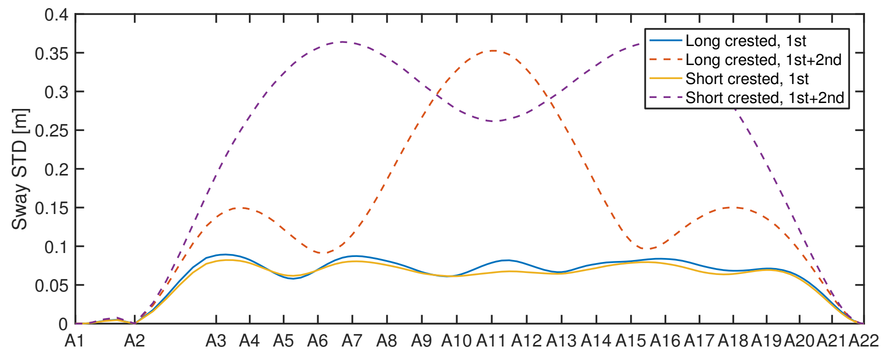

Figure 13: The standard deviation of sway motion along the bridge girder in LC1, LC2, LC4 and LC5 when short-crested waves and second order wave loads are considered and not considered. Waves mainly come from 270°.

loads, which are caused by long-crested waves or by short-crested waves; as a result, the low frequency sway motion is dominant. When the waves are long-crested, only the second eigen mode is excited. Whereas both the first and second eigen modes are excited if the waves are short-crested. Additionally, the eigen modes excited at different points vary under short-crested waves. At A11, it is the second mode that is excited, while the first mode is excited at A16. Both the first and second modes are excited at A12. As the node moves from A11 to A16, the second mode resonant response gradually decreases, and in contrast the first mode resonant response increases.

The heave motion along the bridge girder is also studied. The standard deviation is shown in Fig. 15(a). Here the second order wave loads have negligible effect on the heave motion, this is because heave second order wave load is not included in the numerical simulations. But the short-crested wave gives much larger standard deviation in heave motion than the long-crested wave. Fig. 16(a) presents the power spectrum of heave motion of girder node at A12. It is observed that the eigen modes with a period of about 7.8 s are excited, and these resonant responses are much larger than the wave frequency response. In addition, the short-crested wave causes much larger resonant response than the long-crested wave.

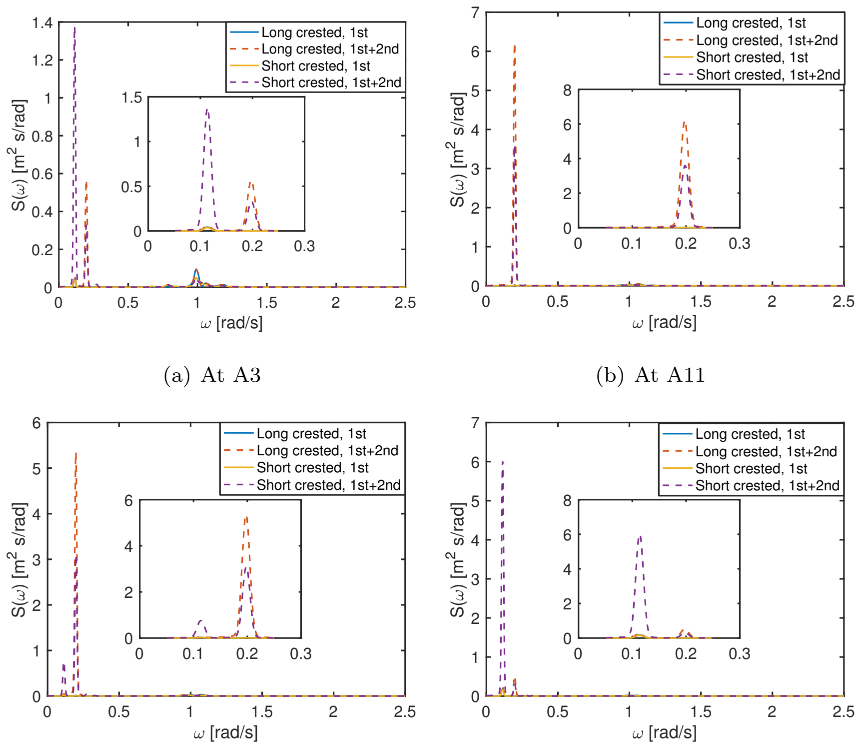

(a) At A3 (b) At A11

(c) At A12 (d) At A16

Figure 14: Spectra of sway motion of girder nodes at (a) A3, (b) A11, (c) A12, (d) A16 in LC1, LC2, LC4 and LC5 when short-crested waves and second order wave loads are considered and not considered. Waves mainly come from 270°.

The weak axis bending moment M_y is mainly induced by the heave motion of girder. Its standard deviation along the girder, as shown in Fig. 15(b), follows similar trend as that of heave motion. The M_y is not affected by the second order wave loads, but is strongly influenced by the short-crested waves. For girder nodes between A3 and A14, the M_y of short-crested waves is almost twice of that of long-crested waves. Power spectral analysis also reveals that it is also due to the excited resonant eigen modes with a period of about 7.8 s.

The standard deviation of axial force, F_x, strong axis bending moment, M_z, and torsional moment, M_x, along the bridge girder is demonstrated in Fig. 17 . By comparing with results considering short crest waves, modeling with long

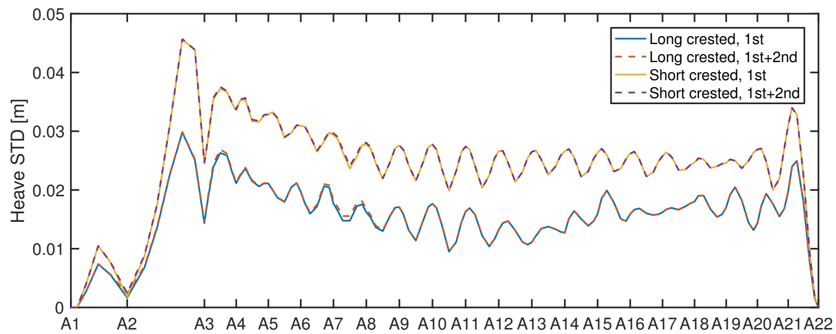

(a) Heave

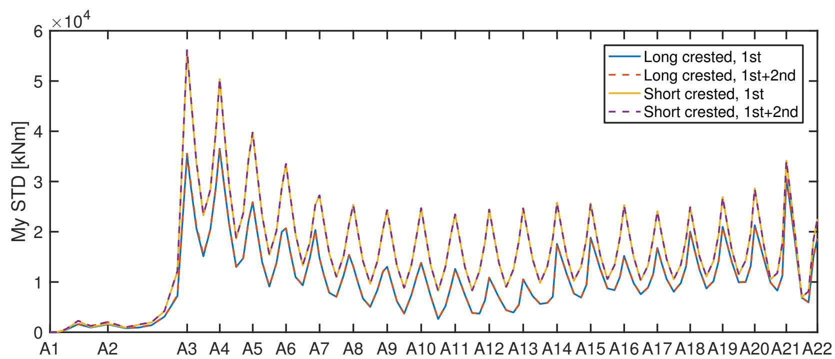

(b) Weak axis bending moment, M_y

Figure 15: The standard deviation of (a) heave motion and (b) Weak axis bending moment M_y along the bridge girder in LC1, LC2, LC4 and LC5 when short-crested waves and second order wave loads are considered and not considered. Waves mainly come from 270°.

crest waves underestimates axial force F_x and strong axis bending moment M_z along the bridge girder. Power spectra were also analyzed to identify the reasons for the difference in responses. Fig. 18 shows the spectra of axial force F_x of girder nodes at (a) A11 and (b) A16. In the vicinity of 1.05 rad/s, long-crested waves cause larger wave frequency responses, while short-crested waves induce larger resonant responses for frequencies ranging from 0.7 to 0.95 rad/s. The difference in responses due to the second order wave loads is more notable between short-crested waves and long-crested waves. The long-crested waves mainly excite the second resonant mode, whereas the short-crested wave excite both the second and third resonant modes.

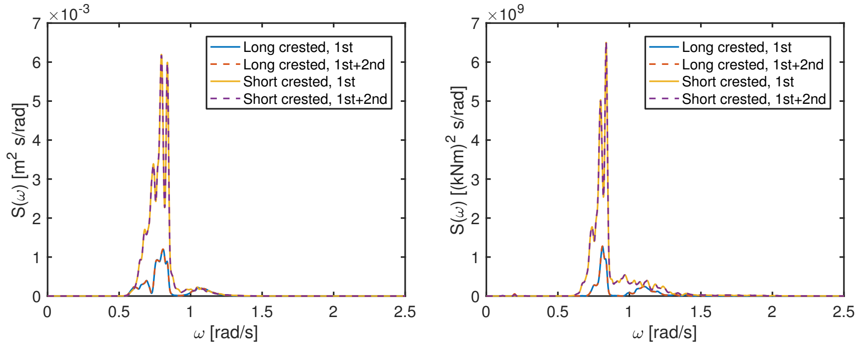

(a) Heave

(b) Weak axis bending moment, M_y

Figure 16: Spectra of (a) heave motion and (b) Weak axis bending moment M_y of girder nodes at A12 in LC1, LC2, LC4 and LC5 when short-crested waves and second order wave loads are considered and not considered. Waves mainly come from 270°.

Fig. 19 shows the spectra of strong axis bending moment M_z of girder nodes at (a) A11 and (b) A16. Similar to the spectra of sway motion in Fig. 14, second order wave loads excite the low-frequency resonant eigen modes. When the waves are long-crested, only the second eigen mode is excited. While both the first and second eigen modes are excited if the waves are short-crested. The wave frequency responses also differ a lot between the short-crested waves and long-crested waves.

Regarding the torsional moment M_x along the girder, the standard deviation is presented in Fig. 17(c). Obviously, it can be found that the M_x is not affected by the second order wave loads. The long-crested waves cause larger M_x at certain locations as well as smaller M_x at others. Power spectral analysis shows that the response of M_x is dominant by resonant responses and wave frequency responses. The resonant responses correspond to a period ranging from 4.5 s to 7.8 s, within which a number of eigen periods are located.

All the above analyses in this section consider waves mainly from 270°, hereinafter, the effect of short-crested waves and second-order wave loads is further analyzed considering waves from 315°. Fig. 20 presents the standard deviation of sway motion along the bridge girder in LC6, LC7 and LC8. Similar to Fig. 13,

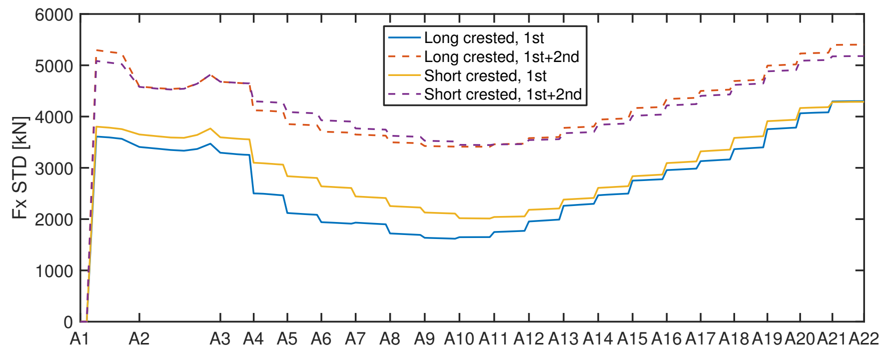

(a) Axial force, F_x

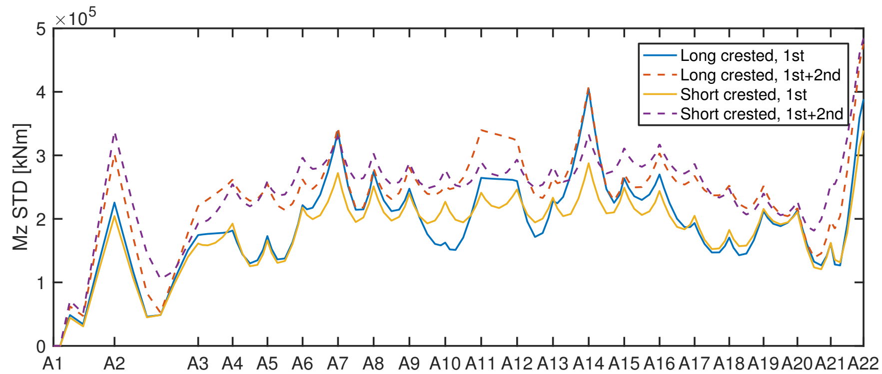

(b) Strong axis bending moment, M_z

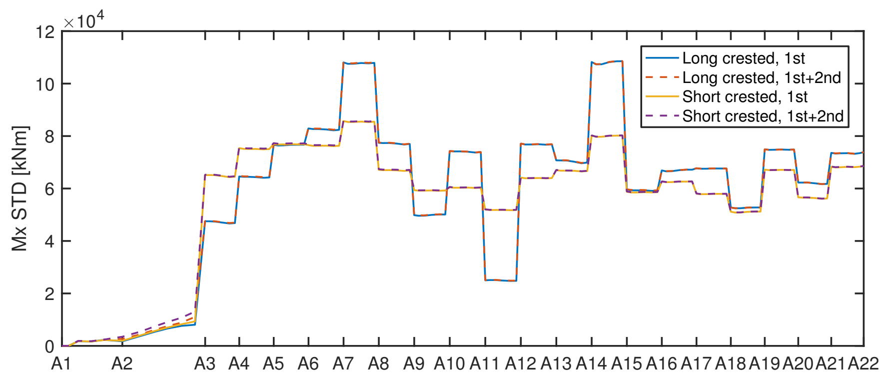

(c) Torsional moment, M_x

Figure 17: The standard deviation of (a) axial force F_x (b) strong axis bending moment M_z, and (c) torsional moment, M_x, along the bridge girder in LC1, LC2, LC4 and LC5 when short-crested waves and second order wave loads are considered and not considered. Waves mainly come from 270°.

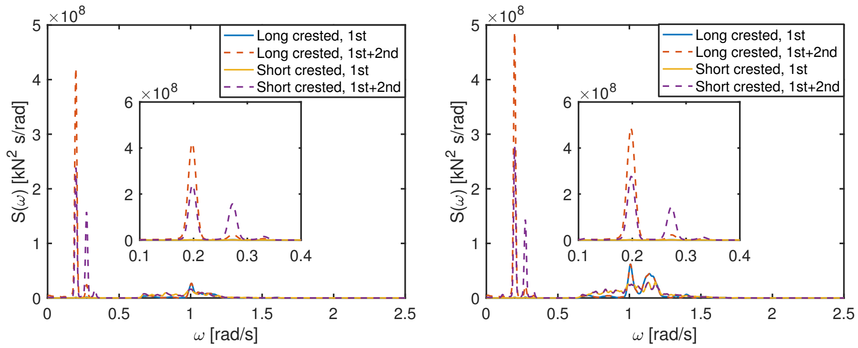

(a) A11 (b) A16

Figure 18: Spectra of axial force F_x of girder nodes at (a) A11 and (b) A16 in LC1, LC2, LC4 and LC5 when short-crested waves and second order wave loads are considered and not considered. Waves mainly come from 270°.

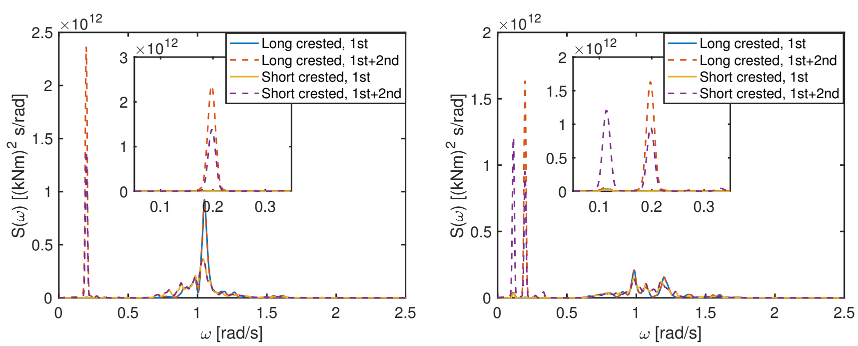

(a) A11 (b) A16

Figure 19: Spectra of strong axis bending moment M_z of girder nodes at (a) A11 and (b) A16 in LC1, LC2, LC4 and LC5 when short-crested waves and second order wave loads are considered and not considered. Waves mainly come from 270°.

the short-crested waves and second order difference frequency forces greatly influence the sway motion, and similar eigen-modes are excited. So do the axial force and strong axis bending moment along the bridge girder. Regarding the standard deviation of heave motion and weak axis bending moment along the bridge girder, the short-crested waves matter a lot while the second order wave loads have negligible impacts.

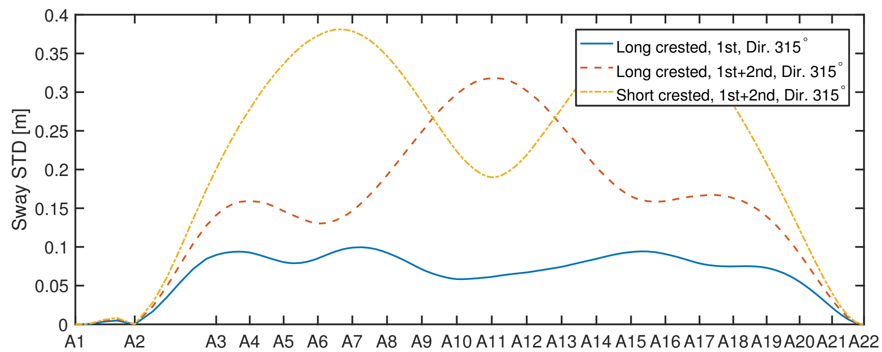

Figure 20: The standard deviation of sway motion along the bridge girder in LC6, LC7 and LC8 when short-crested waves and second order wave loads are considered and not considered. Waves mainly come from 315°.

It should be noted that all results presented in this section are with respect to standard deviations. The discrepancies will be more notable if extreme responses are taken into consideration. Hence, modeling with short-crested wave and with second order wave loads is strongly recommended in the numerical modeling of a floating bridge in a fjord.

7. Conclusions

Designing a floating bridge crossing a wide and deep fjord is very challenging from a technical point of view. The extreme environmental loads and load effects should be properly evaluated for ultimate strength design check. The wave conditions in a fjord are quite different from those in the open sea. Hence, modeling of wave loads for a very long floating bridge in a fjord is very interesting and challenging. By using an early concept of the floating bridge designed for crossing Bjørnafjorden, this study addressed comprehensively several modeling aspects of hydrodynamic loads, including varying water depth, viscous drag forces, short-crested waves and second order wave loads.

The floating bridge concept is an end-anchored curved bridge, about 4600 m long. It consists of a cable-stayed high bridge part and a low bridge part supported by 19 pontoons. A numerical model was built by using the coupled time domain code SIMO-RIFLEX. Eigen-frequencies, eigen-modes and static structural responses in calm water were first analyzed.

Several modeling aspects of hydrodynamic loads were then investigated. It is found that the varying water depth affects hydrodynamic coefficients at low frequencies, and thus has negligible influence on the dynamic responses of the floating bridge considering the wave condition in the fjord. Second order difference frequency wave loads can excite low frequency resonant responses in the sway mode, axial force and strong axis bending moment along the bridge girder. But these resonant responses can be mitigated by viscous drag forces on pontoons. Short-crested waves greatly affect the heave motion and weak axis bending moment along the bridge girder. Both short-crested waves and second order wave loads should be considered when investigating the wave load effect of the floating bridge. So do the viscous drag forces on the pontoons given the viscous drag coefficients are properly estimated.

As a whole, this study deals with the modeling aspects of hydrodynamic loads using the floating bridge which was considered for crossing Bjørnafjorden. The conclusions are acquired based on numerical simulations, their verifications against a model test are also necessary and favorable. The considerations and conclusions are also useful when evaluating the wave load effects for other floating bridges in a fjord. Additionally, as mentioned in this paper, this study assumes homogeneous wave condition, while the wave field in a fjord is usually inhomogeneous. The study serves as a basis when further addressing the wave load effect of a floating bridge under inhomogeneous wave conditions [1].

Acknowledgment

This work was supported by the Norwegian Public Roads Administration and in parts by the Research Council of Norway through the Centre for Ships and Ocean Structures (CeSOS) and Centre for Autonomous Marine Operations and Systems (AMOS), at the Department of Marine Technology, NTNU, Trondheim, Norway. The support is gratefully acknowledged by the authors.

References

[1] Cheng Z, Gao Z, Moan T. Wave load effect analysis of a floating bridge in a fjord considering inhomogeneous wave conditions. Submitted for possible publication 2017;.

[2] Eidem ME. Overview of floating bridge projects in Norway. In: Proceedings of the ASME 2017 36th International Conference on Ocean, Offshore and Arctic Engineering. ASME; 2017,.

[3] Kashiwagi M. A time-domain mode-expansion method for calculating transient elastic responses of a pontoon-type VLFS. Journal of Marine Science and Technology 2000;5(2):89–100.

[4] Fu S, Moan T, Chen X, Cui W. Hydroelastic analysis of flexible floating interconnected structures. Ocean engineering 2007;34(11):1516–31.

[5] Michailides C, Loukogeorgaki E, Angelides DC. Response analysis and optimum configuration of a modular floating structure with flexible connectors. Applied Ocean Research 2013;43:112–30.

[6] Yoon JS, Cho SP, Jiwinangun RG, Lee PS. Hydroelastic analysis of floating plates with multiple hinge connections in regular waves. Marine structures 2014;36:65–87.

[7] Seif MS, Inoue Y. Dynamic analysis of floating bridges. Marine structures 1998;11(1):29–46.

[8] Lu D, Fu S, Zhang X, Guo F, Gao Y. A method to estimate the hydroelastic behaviour of VLFS based on multi-rigid-body dynamics and beam bending. Ships and Offshore Structures 2016;:1–9.

[9] Kvåle KA, Sigbjörnsson R, Øiseth O. Modelling the stochastic dynamic behaviour of a pontoon bridge: a case study. Computers & Structures 2016;165:123–35.

[10] Lie H, Fu S, Fylling I, Fredriksen AG, Bonnemaire B, Kjersem GL. Numerical modelling of floating and submerged bridges subjected to wave, current and wind. In: ASME 2016 35th International Conference on Ocean, Offshore and Arctic Engineering. American Society of Mechanical Engineers; 2016,.

[11] Fredriksen AG, Heiervang MF, Larsen PN, Bonnemaire B, Sandnes PG, Sørby B, et al. Hydrodynamical aspects of pontoon optimization for a side-anchored floating bridge. In: Proceedings of the ASME 2017 36th International Conference on Ocean, Offshore and Arctic Engineering. ASME; 2017,.

[12] Løken AE, Oftedal RA, Aarsnes JV. Aspects of hydrodynamic loading and responses in design of floating bridges. In: Second symposium on strait crossings. Trondheim, Norway; 1990,.

[13] COWI . NOT-HYDA-018 Curved bridge navigation channel in south - environmental loading analysis. Report for the Norwegian Public Road Administration. COWI AS, Oslo, Norway; 2016.

[14] Cheng Z, Svangstu E, Gao Z, Moan T. Field measurements of inhomogeneous wave conditions in Bjørnafjorden. Submitted for possible publication 2017;.

[15] Lothe A, Musch O. Bjørnafjorden submerged floating tube bridge: sea state simulations. Tech. Rep.; Norconsult AS; 2015.

[16] SVV . Design basis metocean. Statens Vegnesen, Norway; 2016.

[17] DNV GL . Enviromental conditions and enviromental loads (DNV-RP-C205). Det Norske Veritas AS, Oslo, Norway; 2014.

[18] MARINTEK . Rifelx theory manual, version 4.0. 2012.

[19] MARINTEK . Simo-theory manual version 4.0. 2012.

[20] Faltinsen OM. Sea loads on ships and offshore structures. Cambridge, UK: Cambridge University Press; 1995.

[21] Cummins WE. The impulse response function and ship motions. Institut fur Schiffbau, Universitat Hamburg, Hamburg; 1962.

[22] Xiang X, Svangstu E, Nedrebø Ø, Jakobsen B, Eidem ME, Larsen PN, et al. Viscous damping modeling of floating bridge pontoons with heaving skirt and its impact on bridge girder bending moments. In: ASME 2017 36th International Conference on Ocean, Offshore and Arctic Engineering. American Society of Mechanical Engineers; 2017,.